Neutron Imaging With Li-Glass Based Multicore SCIntillating FIber (SCIFI)

Neutron imaging with Li-glass based multicore SCIntillating FIber (SCIFI)

Michael E. Moore[a], Pavel Trtik[b], Joris Lousteau[c], Diego Pugliese[d], Gilberto Brambilla[e], Jason P. Hayward[a]

[a] Department of Nuclear Engineering, University of Tennessee, Knoxville, TN 37996, USA
[b] Laboratory for Neutron Scattering and Imaging, Paul Scherrer Institut (PSI), CH-5232 Villigen, Switzerland
[c] Department of Chemistry, Materials Engineering and Chemical Engineering, Politecnico di Milano, Via Mancinelli, 7, 20131 Milano, Italy
[d] Department of Applied Science and Technology, Politecnico di Torino, Corso Duca degli Abruzzi 24, 10129 Torino, Italy
[e] Optoelectronics Research Centre, University of Southampton, Southampton, SO17 1BJ, UK

***Abstract*–The improvement of neutron imaging towards and beyond the microscale is a well-documented need for the iterative characterization and modeling of numerous microstructured X-ray opaque materials. This work presents the recent progress in evaluating a SCIntillating FIber (SCIFI) proof-of-concept towards micron-level thermal neutron radiography. These SCIFIs are composed of ^{6}Li-enriched silicate glass cores doped with a Ce activator. The cores possess ~8.5 µm diameters and ~10 µm pitch following fiber drawing with a cladding glass into an all-solid multicore fiber. A polished 5 mm × 5 mm array of 100 microstructured multicore SCIFI pixels was fabricated into a 1 mm thick faceplate. The neutron efficiency and light yield of the faceplate are characterized as functions of the 7.38 weight percent of Li_2O, thickness, and the 70% active volume. It was determined that approximately 39% of a thermal neutron (2 Å) beam can be absorbed by the faceplate. The $^{6}Li(n,\alpha)t$ reaction is estimated to produce 7,700 ± 1,000 scintillation photons per event, referencing light collection from ^{241}Am irradiation of the faceplate. Simulations suggest that on average 17.5 ± 1.4% of these photons will be transported to an end of the fiber array for a thermal beam, with at least 7.2% of that total scintillation light being confined into the fiber cores in which it originated. The SCIFI faceplate was integrated into the Neutron Microscope (NM) at the Pulse OverLap DIffractometer (POLDI) beamline located at the Paul Scherrer Institut to image a Siemens star test object. Processed neutron radiographs acquired with the proof-of-concept faceplate resolved features at a state-of-the-art resolution of 16.1 ± 0.5 µm. The potential for even high resolution designs having smaller pitch or different cladding material is discussed.**

***Index Terms*–Scintillating Fiber, Neutron Imaging, Multicore Fiber, High Resolution, Enriched Lithium Glass, Optical Waveguides.**

I. Introduction

THE current thrust to improve neutron imaging resolutions towards and beyond the microscale is motivated by the need to support advance neutron scattering facility users in the characterization and modeling of a growing list of novel, microstructured, X-ray opaque materials [1][2]. For example, high resolution neutron imaging supports models of diffusion-based Li transport and crystallographic texture control of metallographic surfaces for the flourishing fields of advanced energy storage and additive manufacturing [3][4]. Incremental improvement for neutron imaging for related applications over the past 2 decades stems from the realization that the spatial resolution of unstructured neutron imagers is fundamentally limited by the variance introduced by charged particles emitted from neutron conversion. Focused development of structured neutron position sensitive detectors, such as patterned powder converter screens and microchannel plates (MCP) accompanied by post processing techniques, like event centroiding, sought to overcome this limitation. Nowadays, advanced neutron scattering facilities are able to resolve features on the order of 10 - 20 µm with the use of state-of-the-art neutron imaging instrumentation [5][6][7]. Yet, continued progress towards micron level imaging remains a challenging goal as the intensity and linearity of thermal neutron fluxes limits radiographic spatial resolution compared to X-ray sources.

In order to increase neutron detection efficiency while improving spatial resolution, we have revitalized the use of SCIntillating FIber (SCIFI) as neutron imagers, and potentially, as neutron conversion charged particle trackers. The SCIFIs are fabricated with the rod-in-tube fiber drawing technique. A Ce doped ^{6}Li enriched silicate glass (Nucsafe Inc., Oak Ridge, TN, USA) that is chemically similar to the well-known GS20 glass is used as the core, and the SCHOTT glass N-KF9 as cladding. These ^{6}Li glass cores have an approximate 8.5 µm diameter and 10 µm pitch following fiber drawing into an all-solid multicore fiber at the University of Southampton's Optoelectronics Research Centre. Nearly 2,700 scintillating ^{6}Li glass cores are contained inside of 1 multicore fiber with a 70% packing fraction inside of the multicore fiber jacket.

Our SCIFI-based neutron radiography relies on thermal neutron attenuation with enriched ^{6}Li. The neutron efficiency and subsequent light yield are functions of the 7.38 weight percent Li_2O as well as the active scintillating volume of glass, and the molar concentration of its constituents. Following thermal neutron absorption on ^{6}Li, an alpha and triton are emitted back-to-back in the $^{6}Li(n,\alpha)t$. For our glass, the track length of the α is ~7 µm and for the t it is ~40 µm [8]. These track lengths are comparable to those found using SRIM-2013 [9] with the composition of aluminosilicate glass defined for GS20 as reported by [8], with the addition of 6.941 weight (amu) of Li, and a compound density of 2.5 g/cm^3. The resulting ionized primary and secondary electrons diffuse through the composite glass matrix with cylindrical radii of ~0.0196 µm and ~0.0648 µm, from the α and t, respectively [10]. Those electrons that escape recombination at the ^{6}Li conversion sites along the saturated track and avoid traps within the glass matrix can induce scintillation by exciting Ce^{3+} centers in the glass cores. Several cores may be partially activated these electrons along the charged particle tracks. The Ce^{3+} emission peak

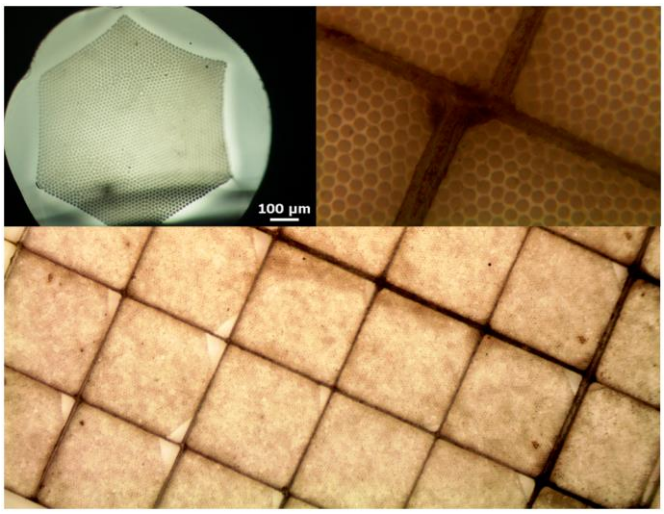

Fig. 1. Microscope photos of the cross section of a microstructured multicore fiber with scale shown (*top left*), the stacked multicore fibers with 8.5 µm core diameters (*top right*), and the polished faceplate surface of a multicore SCIFI array with 0.5 mm x 0.5 mm pixels (*bottom*). [11]

within ^{6}Li-glass is centered at λ ~ 395 nm. The near-UV scintillation is then emitted isotopically into 4π where angle-dependent-refraction totally bounds a percentage of light within the SCIFI. The bound light and the light that is transmitted to the neighboring cores and cladding are then transported to an exit surface of the multicore SCIFI to be read out by an optical system and a camera/CCD/CMOS, illustrated in [11]. A well-polished 5 mm × 5 mm array of 100 microstructured multicore SCIFI pixels was fabricated into a 1 mm thick faceplate, see Fig. 1. The complete fabrication details and initial experimental evaluation of a single multicore SCIFI, as well as related research history are described in our recent paper [11].

In this paper, we report of the characterization of this multicore SCIFI faceplate through a combination of simulations and measurements. Section II describes simulations of the scintillation light transport from thermal neutron conversion and an experimental estimate of the light yield of the SCIFI faceplate. Section III describes our experimental setup for neutron imaging. Section IV presents our imaging resolution results. Section V provides a discussion, as well as our expectations for further development of similar SCIFI neutron imaging instrumentation. Section VI gives conclusions.

II. SCIFI Neutron Imager

The resolution of neutron images produced by the SCIFI is determined in a large part by the capacity of the optical fiber to collect the scintillation light inside of the SCIFI cores. Given that the scintillation wavelength is significantly smaller than the dimensions of the SCIFI multicore, light propagation is effectively modeled in terms of total internal reflection (TIR). When the refractive index of a fiber core, n_{core}, is greater than the refractive index of the fiber cladding, n_{clad}, scintillation light incident on the cladding will be captured into the core through TIR. The difference $n_{core} - n_{clad}$ is associated with a numerical aperture (NA) and a critical angle, θ_c, with respect to the normal of the surface, which determines the fraction of scintillation light guided with the SCIFI core. Modeling the TIR transport process is crucial towards understanding the ultimate potential for even higher resolution designs. In an ideal design, in which $n_{core} \gg n_{clad}$, negligible light transmission into the cladding matrix of the multicore fiber, as well as reduced inter-core cross-talk, would allow for one to image the end of the faceplate and resolve the ^{6}Li glass cores from the cladding with excellent contrast. Such an image would possess a spatial resolution limited by the pitch of the ^{6}Li glass cores at any frequency. In reality, the production of an actively scintillating microstructured multicore fiber requires matching a host of thermal, mechanical, and chemical properties, in addition to selecting ideal refractive indexes [12].

The precise n was measured for a monolithic ^{6}Li glass rod at five different wavelengths (633, 825, 1061, 1312 and 1533 nm) by a prism coupling technique (Metricon, model 2010). Ten scans were performed for each measurement with an estimated error of approximately ± 0.001. The measured refractive index values are reported in Table 1. A 3rd order Sellmeier equation was fitted to the measured refractive indexes (see Fig. 2) to determine the n_{core} for the emission of the Ce^{3+} doped ^{6}Li glass within our simulations:

$$n(\lambda)^2 - 1 = \frac{A\lambda^2}{\lambda^2 - B^2} + \frac{C\lambda^2}{\lambda^2 - D^2} + \frac{E\lambda^2}{\lambda^2 - F^2}$$

where the values $1.285, 1.315 \times 10^{-2}, -1.051 \times 10^{-4}, 3.911 \times 10^{-1}, 1.327 \times 10^{-2}$, and 4.472 were found for A, B, C, D, E, and F, respectively. It was observed that the estimated n_{core} value of 1.55 for Nucsafe ^{6}Li glass matched to the commonly quoted value for GS20 at λ ~ 395 nm. The N-KF9 cladding glass possesses a n_{clad} approximately equal to 1.54 at the peak scintillation emission. Applying Snell's law, the θ_c of the SCIFI waveguide is 83.49°. The other physical properties of N-KF9 (PN 523515.250) can be readily found in SCHOTT's Optical Glass Data Sheets. Again, the specific glass drawing compatibility and fiber pulling process is described in detail in [11].

TABLE I
Refractive Index Values For The ^{6}Li-Glass

Wavelength [nm]	***n* ± 0.001**
633	1.524
825	1.519
1061	1.515
1312	1.512
1533	1.509

A. Simulated light transport within the multicore structure

A model of the total averaged light transport to the exit, or imaged surface, of the faceplate is required in order to estimate an effective light yield. So, light propagation in the multicore architecture was simulated with the ray-tracing software Zemax OpticStudio 15.5 [12]. Three tasks were necessary to model the total light transport through the multicore SCIFI with Zemax: 1) define the materials and draft the architecture, 2) simulate the scintillation light source, transport, and detection, and 3) estimate the average total transported light as a function of distance to the imaged exit of the faceplate.

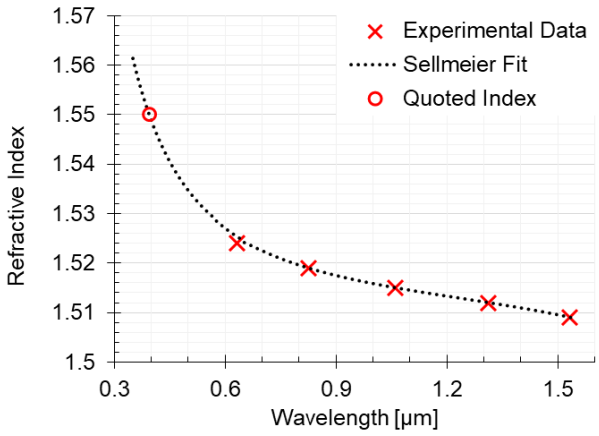

Fig. 2. Sellmeier fit of the measured refractive indexes for the ^{6}Li glass. The error is smaller than the data points (see text).

1) Material definitions and architecture

Using the Sellmeier fit described and the commonly reported density and thermal properties of GS20, the Li-glass material definition was added to the Zemax software material library. The default material definitions for N-KF9 found in Zemax's SCHOTT Material Library were used for the multicore cladding. Two-hundred-seventeen (217) cylindrical volumes of the defined ^{6}Li glass (dimensions of 4.25 μm radius and 1 mm length) were hexagonally packed within the N-KF9 cladding (dimensions of 100 μm radius and 1 mm length) with an 11 μm pitch, see Fig. 3. The ^{6}Li cores were embedded within the cladding material with the exiting ends of cores exposed. A completely absorbing mock imaging surface of dimension 0.2 mm × 0.2 mm was centered 1 μm away from one end of the multicore fiber. The absorbing surface was created with an effective pixel size of 200 nm × 200 nm.

2) Simulated scintillation

Ce^{3+} scintillation light was non-sequentially simulated using volumetric light sources with isotropic emission within the core glass. The light sources possessed discrete wavelengths of 395, 410, and 420 nm that were weighted to represent the observed emission of the SCIFIs, as discussed in more detail later. Mock scintillation along the charged particle tracks was simulated considering columnar light sources with lengths of 7 μm and 40 μm and radii of ~0.0196 μm and ~0.0648 μm, described earlier for the α and t, respectively. The volume of the columnar sources was rotated perpendicular to the length of the multicore fibers. The light from these sources was then non-sequentially transported to the absorbing detector, see Fig. 4. Likewise, the columnar sources were simulated for a scenario in which the charged particles were emitted in the direction parallel with the length of the fibers. For particles produced inside of a core, emitted back-to-back, and simulated by a random orientation of the columnar sources partially ionized an average of 3 ^{6}Li-glass cores. A disk-shaped light source, with a length of 0.02 μm and a radius of 40 μm, was used to simulate the light transport for isotropic emissions from the origin of the model.

3) Light transport

The average total light absorbed at the detector for the disk source, and the sum of the perpendicular and the parallel cases was tallied at incremental distances away from the detector.

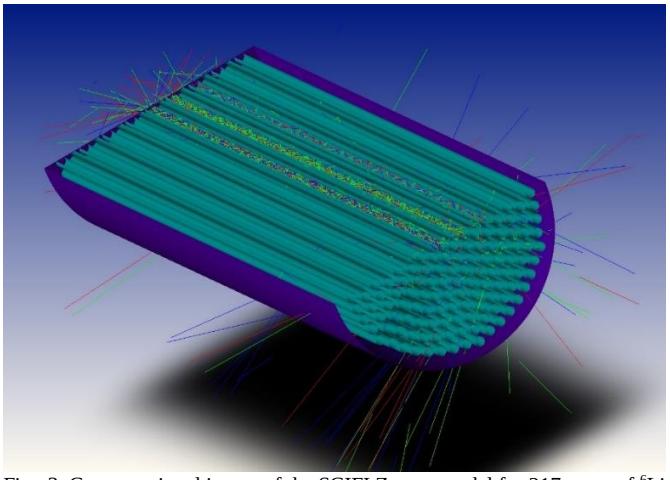

Fig. 3. Cross-sectional image of the SCIFI Zemax model for 217 cores of ^{6}Li glass cores embedded in N-KF9 cladding with mock scintillation light source.

Total light was tallied, not only guided light, to better represent the number of photons incident on the photosensor during light yield measurements. A fit to light transport of these simulated cases was made to estimate the percentage of photons transported to the detector outside of the exit of the fiber for neutron conversion scintillation at any given position within the 1 mm thick faceplate, see Fig. 5. The expected percentage of transported light remains between 50% and 7.2%; the percentage is fundamentally limited by the maximum 2π geometry close in to the detector and the critical angle for TIR light produced 1 mm away from the detector.

B. SCIFI faceplate light yield measurements with ^{241}Am

The total light yield responses from GS20 to either ^{241}Am irradiation or thermal neutron conversion are nearly identical when considering the dominant fast component of the scintillation light decay. This is because the total energy present and able to be transferred via ionized electrons to the supposed uniform concentration of Ce activator sites available in the ionized track volume of a 5.486 MeV alpha has been shown to be comparable to that of a thermal neutron absorption reaction $^{6}Li(n,\alpha)t$ for GS20 glass. Pulse shape and light yield measurements have verified this observation [14]. Thus, the ^{241}Am source could therefore be used to measure light yield from a known ionization location in a scale of minutes compared to the days required for thermalizing the available ^{252}Cf neutron source to record the same number of neutron events captured at random locations. In order to account for any discrepancies between the two yields, a conservative error representative of the difference in ionized volumes is propagated. These ionization volumes have been estimated at $5360 \times 10^{-16} cm^3$ and $4730 \times 10^{-16} cm^3$ for the ^{6}Li absorption reaction and an ^{241}Am alpha, respectively [10]. A linear relationship between the two ionization volumes would underestimate the higher likelihood of recombination for the slower moving 2.04 MeV conversion alpha compared to the 5.486 MeV alpha, and thereby overestimate the potential difference in light yield. Thus, at maximum, one would expect the light yield value of ^{241}Am alpha to be within a 12% error of the $^{6}Li(n,\alpha)t$ reaction.

Light yield measurements were conducted to better understand the specific scintillation properties of the Nucsafe

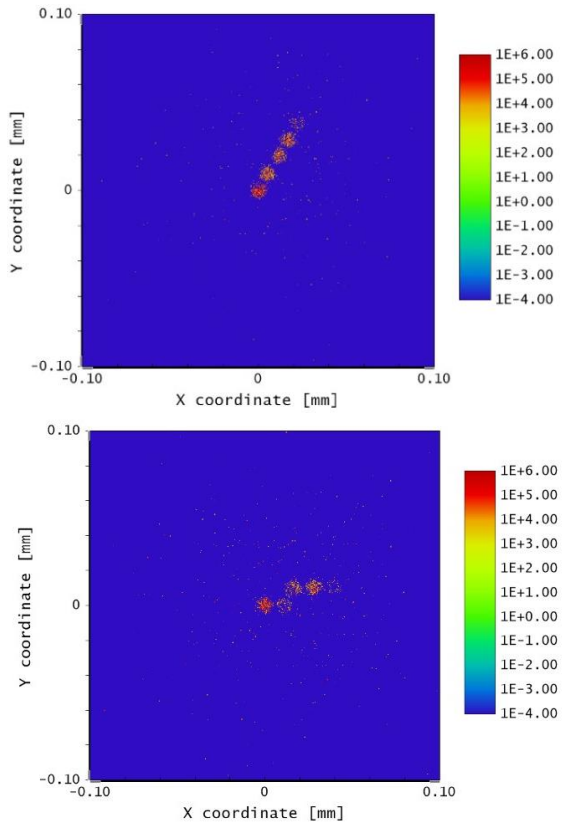

Fig. 4. Simulated charged particle scintillation tracks of the thermal neutron capture on ^{6}Li emitted perpendicular to the multicore fiber 0.522 mm away from the detector at 60° (*top*) and 10° (*bottom*) relative to the abscissa.

^{6}Li glass within the faceplate. To collect the photons, a surface of the SCIFI faceplate was coupled to a R4998 Hamamatsu photomultiplier tube (PMT) with silicone grease. A 1 µCi ^{241}Am source was placed on opposite surface, then both source and faceplate were secured to the PMT window with Teflon tape. Inside of a light tight dark box, the PMT setup was biased to -1825 V and its signals were sent to a CAEN DT 5720 digitizer. The waveforms from individual alpha events were collected with a 300 ns window. Comparison between the energy histogram obtained from the waveforms revealed that X-rays from the ^{241}Am source contributed to approximately 0.97% of the total integrated charge. The integral charge of 260,000 alpha waveforms was then averaged to obtain an average integrated charge collected from the SCIFI faceplate in response to a 5.486 MeV alpha. It was found that an integrated charge, C_{int}, of 16.7 $\pm$ 0.2 pC could be expected per alpha.

Digitized reference plots for the PMT's gain, G_{PMT}, radiant sensitivity, RS, and quantum efficiency, QE, and the previously measured radioluminescence response of the faceplate, were used to estimate an average number of photons collected at the PMT window across the emission spectrum, see Fig. 7. The peak emission wavelength of the SCIFI faceplate is 405 nm, as seen in the radioluminescence spectrum, which is near to the typical emission of Ce^{3+} for GS20 scintillating glass. Zemax simulations of columnar light sources 23 µm in length, representative of the 5.486 MeV alphas, were run to determine the expected percentage of photons that are transported from the alpha event to the photodetector. For this case, it was estimated that an average light transport, LT, of 7.4% of the

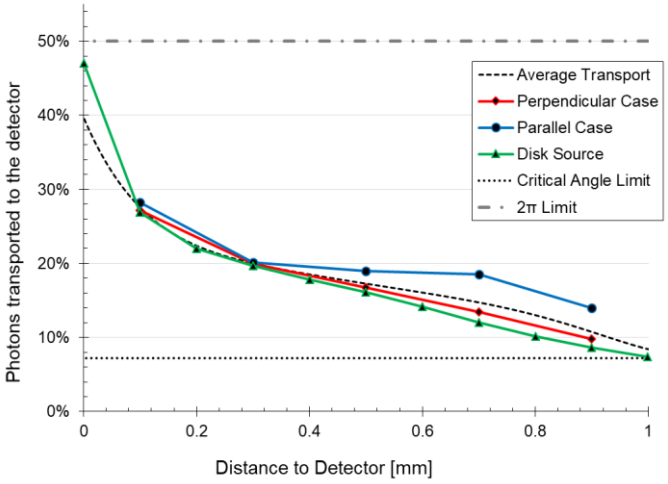

Fig. 5. Simulated light collection for averaged charged particle emissions for various geometries as a function of distance transported.

scintillation photons would reach the PMT window. Thus, light yield was estimated by

$$LY = \frac{C_{int}}{G_{PMT} \cdot e \cdot QE \cdot RS \cdot LT}$$

where G_{PMT} is 1.2×10^{6}, QE is 20.6%, RS is 74%, and the charge constant of an electron, e, is $1.602 \times 10^{-19} C$. LY was estimated at ~7,700 photons per 5.486 MeV alpha. Thus, we would expect to collect 7,700 ± 1,000 photons per thermal neutron conversion. Nucsafe's ^{6}Li glass is reported at a 15-30% higher light output as compared to the 6,000 photons per thermal neutron conversion that is frequently cited for GS20 [15]. It should also be noted that the ionization energy lost by the ^{241}Am alpha to the cladding glass is assumed to be equivalent to the energy lost by the conversion particles in the SCIFI faceplate due to the random trajectories both encountering the same packing fraction.

C. Neutron conversion photons

The neutron conversion efficiency of the SCIFI faceplate was determined empirically in basic terms using the dominant $^{6}Li(n,\alpha)t$ absorption cross section, σ_{abs}, of 940 barns ($10^{-24}\ cm^2$) for 2 Å wavelength thermal neutrons. The attenuation is expressed by the Beer-Lambert law, $I = I_0 exp^{(-\Sigma \mu_i x_i)}$, where I_0 and I are the incident flux and transmitted flux of neutrons at iteration i, at x thickness for an attenuation coefficient µ. The attenuation coefficient is calculated as $\mu_i = \sigma_{tot} N_A c_i$, where σ_{tot} is the total thermal neutron cross section for the SCIFI faceplate, N_A is Avogadro's Number, and c_i is the molar concentration at i. Because the ^{6}Li absorption cross section is dominant, it is assumed that σ_{tot} is $\sim \sigma_{abs}$ of ^{6}Li. Referencing the 7.38 weight percent Li_2O at a 95% ^{6}Li enrichment and 2.5 g/cm^3 density, the concentration of ^{6}Li atoms in the Nucsafe core glass is ~$7.575 \times 10^{21} atoms/cm^3$. So, the attenuation coefficient is $7.121\ cm^{-1}$. We note here that Nucsafe glass has nearly half of the ^{6}Li atom centration that is typically reported for GS20, resulting in an attenuation coefficient value of roughly half. Recalling the ~0.7

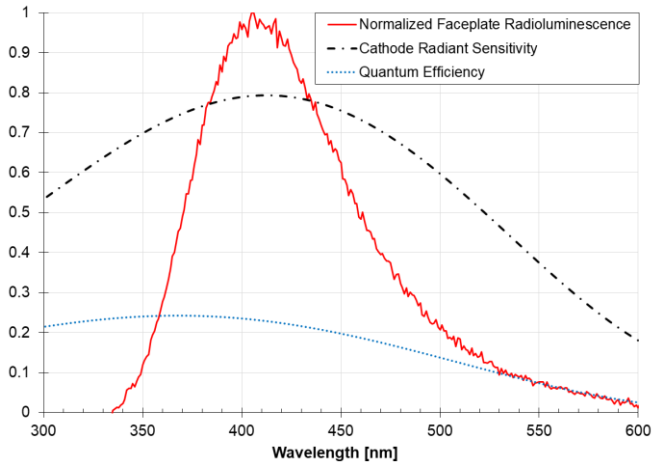

Fig. 7. Normalized SCIFI faceplate radioluminescence plotted against the specific QE and radiant sensitivity of the PMT.

active volume at any given cross-section the attenuation of the SCIFI faceplate for a thermal neutron beam is,

$$\frac{I}{I_0} = exp^{(-0.7 \cdot 7.121\ cm^{-1} \cdot 0.1)}$$

Since the thickness of the faceplate is 0.1 cm, one would expect 39% of the thermal neutron beam to be absorbed in the detector. Further, the average depth of neutron absorption is about 0.479 mm into the SCIFI or 0.521 mm away from the imaging surface of the detector. Plotting the average light transport fit against neutron attenuation, it is found that ~17.5% of the 7,700 scintillation photons will reach the imaging surface of the SCIFI at the average depth of neutron absorption, see Fig. 6.

III. Experimental Setup

The SCIFI faceplate was imaged at the Pulse OverLap DIffractometer (POLDI) beamline at the Swiss Spallation Neutron Source (SINQ) hosted by the Paul Scherrer Institut (PSI). POLDI utilizes a thermal neutron spectrum of 1.1– 5 Å with a maximum flux at the imaging target of about $10^8\ n/s/cm^2$, where the beam aperture was adjusted to provide a L/D ratio of ~240 [16]. The Neutron Microscope (NM), a high resolution and numerical aperture optical microscope, was used to image our SCIFI faceplate. Distinctively, the NM possesses a magnification and numeric aperture, described in [17][18], that enables a nominal pixel size of acquired images down to 1.3 µm, and a true spatial resolution of about 5 µm. The faceplate was substituted in for the gadolinium oxysulfide ($^{157}Gd_2O_2S$:Tb) (Gadox) scintillating screen typically used with the NM [19]. Due to the thickness increase of the SCIFI faceplate compared to the Gadox screen developed for the framework of the NM, focusing on the end of the faceplate was nontrivial. As done previously [11], a diffused blue light source was used to optically focus the microscope onto the imaging surface of the faceplate. After optical focusing, Al tape was used to seal the faceplate in the light-tight adaptor for imaging.

With the SCIFI in place, the dark field (DF) and open beam (OB) images of the scintillator alone were first acquired. DF and OB acquisitions are images of the scintillator sealed within the light tight adaptor without an imaging object with the neutron beam shutter closed and shutter open, respectively.

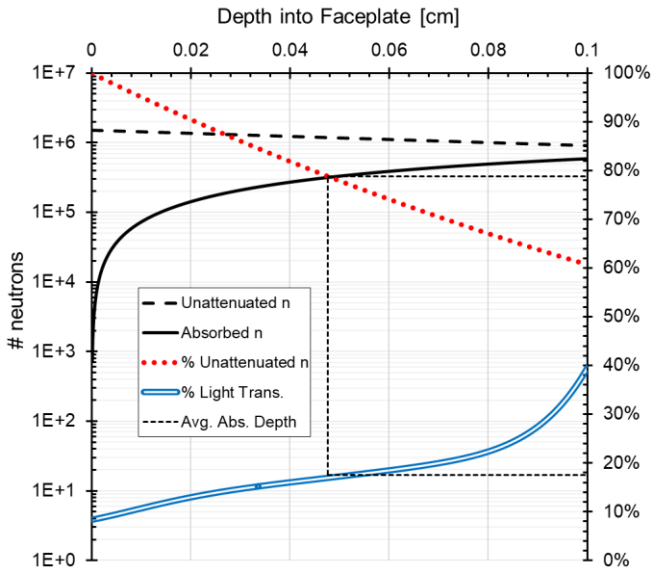

Fig. 6. Thermal neutron attenuation as a function of depth into the SCIFI faceplate plotted against the fit of average light transport to the imaging surface of the simulated detector.

These images are acquired to reduce the influence of the neutron beam intensity gradient, background radiation, inhomogeneity of the faceplate, and inherent imaging readout noises on the resolution of the neutron radiographs during post processing. In order to match the beam shape for the aperture slit positions for a 240 L/D ratio, the acquired field of views were down selected from the possible 5.5 × 5.5 mm to 2.6 × 4.4 mm, corresponding to 936×1584 pixels in the *x* and *y* directions, where a $2.\overline{77}$ µm effective pixel size was calculated from the acquired images. Two DF images and 120 OB radiographs were acquired with 300 s exposures at a 50 kHz and 16-bit readout rate. A large number of OB images were taken to compensate for the pulsed mode of SINQ that shares the high intensity proton accelerator beam for the production of ultracold neutrons, and other fluctuations in the beam current. A PSI Siemens star neutron imaging test target was then positioned directly in front of the Al capped SCIFI faceplate [20]. Seventy-five (75) neutron radiographs of the star were acquired with 300 s exposures for a total exposure time of 375 min.

IV. Results

ImageJ software, an open source scientific image analysis tool, was used to process the acquired images [21][22]. Background radiation at the beamline and cosmic interactions with the CCD camera often speckle neutron radiographs with comparatively high grey count values in relative small pixel areas. To remove bright outliers from these interactions, all images compared a median grey count value of a 2 pixel neighboring radius of every pixel to a 25 grey count threshold for deviation. If a pixel exceeded this threshold, then it was replaced with the median value of the neighboring pixels. The DF and OB images were processed first to make the previously described corrections. After removing the bright outliers from the 2 DF image stack and the 120 OB image stack, each stack was projected to create a third *z* axis with ImageJ. The so-called *z* projections allow one to compare the value of a pixel at a

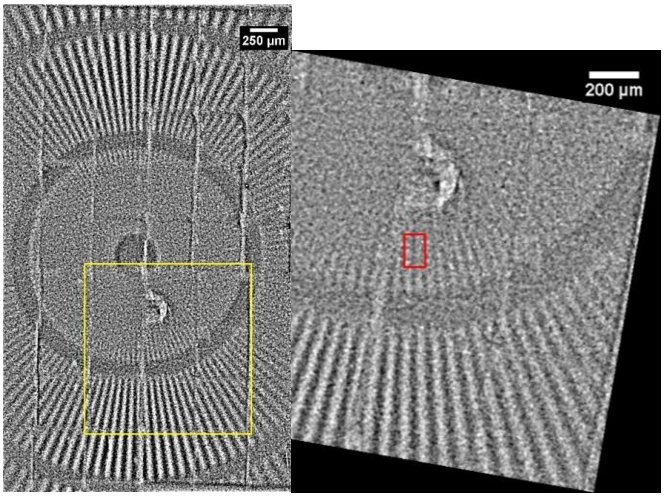

Fig. 8. Neutron radiograph of PSI's gadolinium-based Siemens star processed with a Fourier Filter (*left*), and an enlarged region of interest with ~16 µm feature highlighted (*right*).

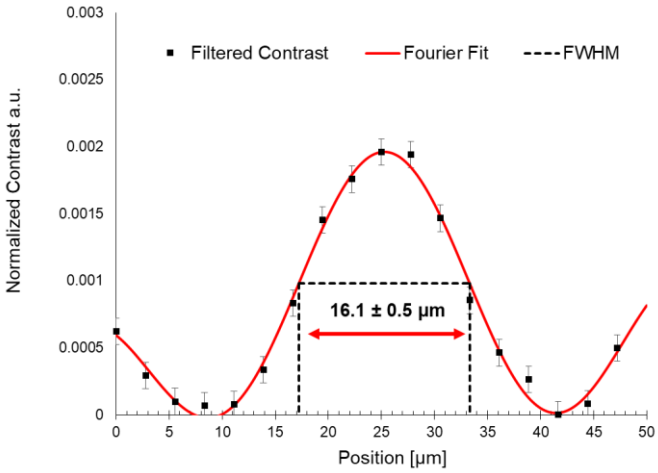

Fig. 9. Line spread Fourier fit of measured contrast for resolved Siemens Star spoke with the FWHM denoted for the filtered radiograph.

specific *x* and *y* location to all of the other pixels at that same location across the stack of images, i.e. across the *z* axis. The *z* projection for the median grey count of every pixel, or the median image, was created for the DF and OB stacks. Next, the bright outliers for the 75 radiographs of the Siemens Star were removed in the same way described above. Then each image in the radiograph stack was divided by the intensity of the median DF and OB images' pixel grey count values. The sum of the *z* projection for the resulting stack of background corrected radiographs was then calculated to create a 300 s normalized radiograph of the star.

The isotropic resolution across the SCIFI can be estimated at ~25 µm by inspecting the resolved features of the resulting radiograph, see Fig. 8 (*left)*. A Fourier transform bandpass filter was used to smooth the radiograph by directionally blurring large and small structures separately. To extract a definitive maximum spatial resolution for the SCIFI faceplate, the highlighted region of the radiograph was transformed with a bilinear clockwise rotation of 10° and analyzed for the unfiltered and filtered image, Fig. 8 (*right*). The inverted contrast of the highlighted Siemens star spoke was summed across the pixels in the *y* direction and plotted against the *x* distance with an error associated with the rotation and filtering. Ultimately, full width half maximum (FWHM) of 17.9 $\pm$ 0.4 µm and 16.1 $\pm$ 0.5 µm were obtained from Fourier peak fits to the spoke's line spread for both the unfiltered and filtered radiograph, respectively, see Fig. 9.

V. Discussion and Outlook

The Zemax transport model described represents averaged values for scintillation light emission. For example, while it is most likely that 3 ^{6}Li-glass cores will be partially ionized by the charged particles from the $^6Li(n,\alpha)t$ reaction, the number of cores can range between 1 and 6. As the number of ionized cores increases, the amount of ionization energy lost also increases as the particles travel through greater distances of cladding. So, in the unlikely event that 6 cores are ionized, the total number of scintillation photons produced is lessened and divided amongst more cores. A similar situation occurs when alphas are produced close to the "wall" of a core, and are emitted towards one of the cladding vertices of the hexagonal packing structure. However, such situations have a small impact on the averaged light emission since they represent rare events. So, the TIR transport model may be used to anticipate the photon collection of future iterative designs of the SCIFI with smaller core pitch or in the case of thicker faceplates. However, a full modal analysis is still required to describe the superposition of propagating modes with a mode field diameter, which differs from the physical geometrical dimensions resulting in light coupling between different cores. Integrating this understanding of transport with future background sensitivity and inter-core optical cross-talk studies will be crucial towards deconvolving charged particle tracks with advanced post processing techniques as described in [23].

The unfiltered spatial resolution measured is roughly equal to twice the pitch of the core packing. The ratio of the TIR light to simulated average total light is approximately equal to 7.2:17.5. In theory, this would suggest that at ~50% of the modulation transfer function, a similar multicore design with a core pitch of 500 nm would be capable of resolving features on the order of 1 µm. Beside the scale of the architecture, the proof-of-concept design itself has ample room for optimization. For example, the current design could be improved upon by simply adding a reflective coating to the surface of the faceplate that is not imaged. Although not as simple, selecting a compatible optical cladding with a lower n_{clad} value would increase the contrast of the multicore fiber. An increase in single core numerical aperture would not only enhance light collection in individual cores, but it would also reduce any intercore optical crosstalk. Both of these features could improve the imaging performance of the SCIFI. Additionally, the possibility of directly coupling a optic SCIFI taper to a readout chip, imaging window, or even MCP touts potential light collection efficiencies that will be ever more important as the imaging community continues to probe increasingly smaller scales. Finally, event centroiding and deconvolution of particle tracks inside the multicore are post processing abilities that may also be applied to further improve the spatial resolution of an optimized light-guiding SCIFI neutron imager.

While currently limited primarily by the long exposure times required to overcome measured low contrast, the all-solid-state SCIFI design performs near to the current state-of-art spatial resolutions without event centroiding or other complex post

processing techniques. Of course, the SCIFI-based radiography that we have demonstrated is one of several approaches for the advancement towards and beyond microscale neutron imaging. The use of scintillating screens, such as ^{6}LiF/ZnS and Gadox, coupled to image intensifying optical setups for high spatial resolution neutron imaging is popular among advanced neutron scattering user facilities due to their high neutron conversion efficiency and excellent light yield [19] [24][25]. Additionally, neutron sensitive MCPs have become more common for high resolution setups, and have been successfully combined with Timepix and Medipix active sensor readouts for high temporal and spatial resolution measurements [26][27][28]. Yet, SCIFIs remain a cost effective, scalable, and neutron efficient imaging tool with a promising outlook for the future.

VI. Conclusion

We have described the characterization of a SCIFI array via measurements and simulations in an effort to understand its current performance and the future potential for similar designs. The $^{6}Li(n,\alpha)t$ reaction light yield of 7,700 ± 1,000 photons per event was estimated with ^{241}Am irradiation of the faceplate for the Nucsafe glass. This measurement confirms that the expected light yield of the ^{6}Li glass has not deteriorated during multicore fabrication. Neutron radiographs of a PSI Siemens Star neutron imaging test target yielded an isotropic spatial resolution of ~25 µm of across the imaging surface of the SCIFI with 375 minutes of exposure. Here both the spatial and temporal resolution suffered from a nonuniform pixel stacking/polishing within the faceplate. However, specific regions of the faceplate resolved sub-20 µm features. The ultimate resolution for the ^{6}Li glass SCIFI faceplate of ~16 µm was determined by fitting the line spread of these features with a Fourier peak fit. To the authors' knowledge, this resolution is the best reported result for a ^{6}Li-glass-based or a multicore SCIFI-based neutron imager.

Acknowledgements

This work was supported by the U.S. Department of Energy, Office of Science, Office of Basic Energy Sciences, under Early Career Award no. DE-SC0010314, and by the Future Photonics Hub (UK EPSRC grant EP/N00762X/1). Neutron imaging experiments were performed at the Swiss spallation neutron source (SINQ), Paul Scherrer Institute, Villigen, Switzerland. The author would like to express his gratitude to Ken Weston at Nucsafe, Inc. Oak Ridge, TN, for providing data relevant to the ^{6}Li-glass characterization.

References

[1] I.S. Anderson, R.L. McGreevy, and H.Z. Bilheux. "Neutron imaging and applications." *Springer Science and Business Media* 200.2209 (2009): 987-0.

[2] N. Kardjilov, et al. "New trends in neutron imaging." *Nuclear Instruments and Methods in Physics Research Section A: Accelerators, Spectrometers, Detectors and Associated Equipment* 605.1-2 (2009): 13-15.

[3] J.Nanda, et al. "Anomalous discharge product distribution in lithium-air cathodes." *The Journal of Physical Chemistry C* 116.15 (2012): 8401-8408.

[4] R.R. Dehoff, et al. "Site specific control of crystallographic grain orientation through electron beam additive manufacturing." *Materials Science and Technology* 31.8 (2015): 931-938.

[5] T. Minniti, et al. "Towards high-resolution neutron imaging on IMAT." *Journal of Instrumentation* 13.01 (2018): C01039.

[6] M. Morgano, et al. "Unlocking high spatial resolution in neutron imaging through an add-on fibre optics taper." *Optics Express* 26.2 (2018): 1809-1816.

[7] A.S. Tremsin, et al. "Neutron radiography with sub-15 µm resolution through event centroiding." *Nuclear Instruments and Methods in Physics Research Section A: Accelerators, Spectrometers, Detectors and Associated Equipment* 688 (2012): 32-40.

[8] A.R. Spowart. "Neutron scintillating glasses: Part 1. Activation by external charged particles and 304 thermal neutrons." *Nuclear Instruments and Methods* 135 (1976): 441-453.

[9] J. Ziegler, J. Biersack, M. Ziegler, The Stopping and Range of Ions in Matter, SRIM, 2013, http://www.srim.org, (2013).

[10] L. Katz and A.S. Penfold. "Range-energy relations for electrons and the determination of beta-ray end-point energies by absorption." *Reviews of Modern Physics* 24.1 (1952): 28.

[11] M.E. Moore, et al. "Fabrication and experimental evaluation of microstructured ^{6}Li silicate fiber arrays for high spatial resolution neutron imaging." *Nuclear Instruments and Methods in Physics Research Section A: Accelerators, Spectrometers, Detectors and Associated Equipment* (2018).

[12] J.S. Sanghera, et al. "Development of low-loss IR transmitting chalcogenide glass fibers." *Biomedical Optoelectronic Instrumentation*. Vol. 2396. International Society for Optics and Photonics, 1995.

[13] OpticStudio, Zemax. "15.5." *Zemax LLC, Seattle, WA* (2016).

[14] E.J. Fairley, and A.R. Spowart. "Neutron scintillating glasses part III pulse decay time measurements at room temperature." *Nuclear Instruments and Methods* 150.2 (1978): 159-163.

[15] Weston, Ken. Message to the author. 11 January 2019. E-mail.

[16] U. Stuhr, et al. "Time-of-flight diffraction with multiple frame overlap Part II: The strain scanner POLDI at PSI." *Nuclear Instruments and Methods in Physics Research Section A: Accelerators, Spectrometers, Detectors and Associated Equipment* 545.1-2 (2005): 330-338.

[17] P. Trtik, et al. "Improving the spatial resolution of neutron imaging at paul scherrer institut–the neutron microscope project." *Physics Procedia* 69 (2015): 169-176.

[18] P. Trtik and E.H. Lehmann. "*Progress in High-resolution Neutron Imaging at the Paul Scherrer Institut-The Neutron Microscope Project." Journal of Physics: Conference Series*, vol. 746. No. 1. IOP Publishing, 2016.

[19] P. Trtik, and E.H. Lehmann. "Isotopically-enriched gadolinium-157 oxysulfide scintillator screens for the high-resolution neutron imaging." *Nuclear Instruments and Methods in Physics Research Section A: Accelerators, Spectrometers, Detectors and Associated Equipment* 788 (2015): 67-70.

[20] C. Grünzweig, et al. "Highly absorbing gadolinium test device to characterize the performance of neutron imaging detector systems." *Review of Scientific Instruments* 78.5 (2007): 053708.

[21] C.A. Schneider, W.S. Rasband, and K.W. Eliceiri. "NIH Image to ImageJ: 25 years of image analysis." *Nature methods* 9.7 (2012): 671.

[22] T. Ferreira, and W. Rasband. "ImageJ user guide." *ImageJ/Fiji* 1 (2012).

[23] Y. Song, et al. "Monte Carlo simulation of a very high resolution thermal neutron detector composed of glass scintillator microfibers." *Applied Radiation and Isotopes* 108 (2016): 100-107.

[24] N. Kardjilovet et al. "A highly adaptive detector system for high resolution neutron imaging." *Nuclear Instruments and Methods in Physics Research Section A: Accelerators, Spectrometers, Detectors and Associated Equipment* 651.1 (2011): 95-99.

[25] L. Santodonato, et al. "The CG-1D neutron imaging beamline at the oak Ridge National Laboratory high flux isotope reactor." *Physics Procedia* 69 (2015): 104-108.

[26] A.S. Tremsin, et al. "High-resolution neutron radiography with microchannel plates: Proof-of-principle experiments at PSI." *Nuclear Instruments and Methods in Physics Research Section A: Accelerators, Spectrometers, Detectors and Associated Equipment* 605.1-2 (2009): 103-106.

[27] A.S. Tremsin, et al. "Digital neutron and gamma-ray radiography in high radiation environments with an MCP/Timepix detector." *Nuclear Instruments and Methods in Physics Research Section A: Accelerators, Spectrometers, Detectors and Associated Equipment* (2018).

[28] R.O. Nelson, et al. "Neutron Imaging at LANSCE—From Cold to Ultrafast." *Journal of Imaging* 4.2 (2018): 45.